electronics

MDPI

Article

Optimization of the Sensitivity of a Double-Dot Magnetic Detector

Massimo Macucci [1], Paolo Marconcini [1,*] and Stephan Roche [2,3]

[1] Dipartimento di Ingegneria dell'Informazione, Università di Pisa, Via G. Caruso 16, I-56122 Pisa, Italy; m.macucci@mercurio.iet.unipi.it

[2] Catalan Institute of Nanoscience and Nanotechnology (ICN2), CSIC and BIST, Campus UAB, Bellaterra, 08193 Barcelona, Spain; stephan.roche@icn2.cat

[3] ICREA – Institució Catalana de Recerca i Estudis Avançats, 08010 Barcelona, Spain

* Correspondence: p.marconcini@iet.unipi.it

Received: 24 May 2020; Accepted: 9 July 2020; Published: 12 July 2020

Abstract: We investigate, by means of numerical simulations, the lowest magnetic field level that can be detected with a given relative accuracy with a sensor based on a double-dot device fabricated in a high-mobility two-dimensional electron gas. The double dot consists of a cavity delimited by an input and an output constriction, with a potential barrier exactly in the middle. In conditions of perfect symmetry, a strong conductance enhancement effect appears as a consequence of the constructive interference between symmetric trajectories. When the symmetry is broken, for example by the presence of an applied magnetic field, this enhancement effect is suppressed. We explore the design parameter space and assess the minimum magnetic field value that can be measured with a given accuracy in the presence of flicker noise.

Keywords: magnetic sensor; quantum dot; flicker noise; mesoscopic cavity

1. Introduction

We have previously reported a somewhat counterintuitive effect [1–3] that consists of the conductance enhancement that can be observed, as a result of constructive path interference, when two constrictions are added around a potential barrier, within an electron waveguide. The two symmetric constrictions, instead of further lowering the conductance, lead to its increase, by up to about an order of magnitude [2].

This phenomenon can be explained describing transport in terms of the semi-classical paths through the device [2]. Every path impinges one or more times against the barrier (sometime being transmitted and other times being reflected) and hits against the cavity boundary, which reflects it. If the tunnel barrier is exactly in the middle of the cavity, several of these paths, being mirror-symmetric with respect to the tunnel barrier and corresponding to an accumulation of the same phase by the electrons, interfere constructively. An example is given by the two mirror-symmetric paths that are traced in red and blue in Figure 1: both of them impinge twice against the tunnel barrier, the red one crosses the barrier the first time and it is reflected the second time, while the blue path is first reflected and then transmitted by the barrier. This constructive interference among paths enhances the conductance of the structure with respect to the case of the barrier alone, but disappears if the symmetry is broken, for example, by shifting the barrier away from the central position, because in that case no mirror-symmetry exists any more.

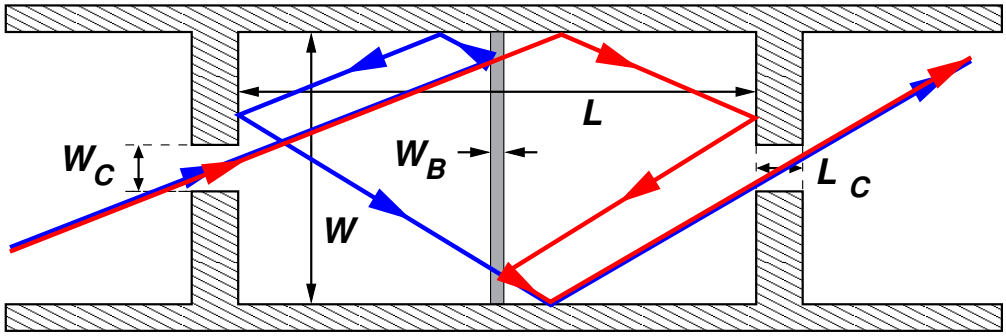

Figure 1. Cavity defined by two constrictions, with a potential barrier in the middle. The red and blue lines represent two mirror-symmetric transport paths which constructively interfere.

Also the presence of a magnetic field orthogonal to the cavity plane introduces an asymmetry (due to the different effect on the phase of the right-going and left-going paths), and therefore suppresses the conductance enhancement effect. Thus, we proposed [4] to exploit this effect for the detection of magnetic fields, in particular in experimental contexts in which a high-quality 2D electron gas at low temperature is already available.

Here we perform an optimization of the device structure, exploring the parameter space in terms of constriction widths, barrier transparency, cavity dimensions, and the possible addition of a magnetic field bias in order to reach the highest achievable sensitivity.

We then discuss the minimum magnetic field value that can be measured with a given accuracy: the main limitation is represented by flicker noise [4], as a consequence of the quadratic dependence of its power spectral density on the bias current. Since the signal power also increases with the square of the bias current, in the presence of flicker noise the signal-to-noise ratio cannot be improved by raising the bias current, contrary to what happens in the case of thermal noise (whose power spectral density is substantially independent of the bias current) and of shot noise (whose power spectral density increases linearly with the bias current). In addition, the variance of the measurement results that is induced by flicker noise cannot be reduced by filtering or averaging, as we will discuss in the following. From the existing experimental literature, we obtain realistic values for the estimates of the flicker noise produced by the constrictions, and use them to assess the overall flicker noise of the device.

We consider also the reduction in the output signal due to Coulomb scattering that results from ionized dopants and charged impurities, which perturb the symmetry of the device. To this purpose, we perform a calculation of the potential landscape due to charges located at a distance of 40 nm from the two-dimensional electron gas (2DEG), corresponding to the typical depth of a spacer layer, and we tune the density of the randomly placed charges in such a way as to obtain a mean free path corresponding to that of the best available 2DEGs.

The paper is organized as follows: in Section 2, we present the device structure and provide some information about the adopted simulation procedure (a complete description of the simulation approach can be found in the cited references); then, in Section 3, we report the results of simulations performed varying the overall cavity dimensions, the barrier thickness, the barrier position, and the constriction width; in Section 4, we present the procedure to obtain a disordered potential yielding the same mean free path as for the best available GaAs/AlGaAs (gallium arsenide/aluminium gallium arsenide) heterostructure and we then study the effect of such a potential on the characteristics of our device; in Section 5 we discuss how the value of the minimum measurable magnetic field is affected by the variance due to flicker noise and obtain an estimate of the minimum magnetic field variation that can be reliably detected.

2. Device Structure and Numerical Method

The device structure that we have considered is sketched in Figure 1: it consists of a rectangular cavity of length L and width W, defined by two symmetric constrictions of width W_C and extending for a length L_C each. In the middle of the cavity we have a potential barrier of thickness W_B and height H_B. A practical implementation of the device, based on a two-dimensional electron gas in a GaAs/AlGaAs heterostructure, would require the lithographic definition of depletion gates creating the lateral confinement and defining the constrictions, as discussed in detail in Reference [5]. There should also be a transverse gate [5] which creates the barrier, whose height can be adjusted simply by tuning the gate bias voltage. It would be possible to exploit the boundaries of a mesa for the lateral confinement, as in Refs. [6,7], and to use depletion gates only for the definition of the constrictions; however, there would be fewer adjustable voltages, which are instead important to compensate possible geometric asymmetries.

In the numeric analysis presented here, we assume, for the purpose of computational efficiency, a hard wall structure exactly coincident with the one represented in Figure 1: the potential is zero in the white regions, infinite in the dashed regions, and equal to 45 meV in the dark-gray barrier area. For the application of our numerical technique, the input and output leads (of a finite length in the sketch of Figure 1) are assumed to be infinitely long.

The assumptions of hard walls and rectangular geometry for the cavity do not significantly affect the general validity of our conclusions, because, as we [8] and other authors [9] have shown in the past, the shape (as well as the exact nature of the walls) of the cavity has no relevant effect on its transport characteristics, contrary to what had sometimes been hypothesized in the literature [10], on the basis of the assumed relevance of the classically chaotic or regular shape. Indeed, all the "chaotic" effects that can be observed in the behavior of conductance and shot noise in such cavities are the result of wavefunction diffraction at the apertures; therefore, they only depend on the presence of significant width variations and not on the overall cavity shape.

We cannot make a direct comparison of our results to experimental data, because the proposed device has not yet been fabricated, but we are confident in the validity of our numerical techniques, because, in the past, they have successfully reproduced [11] the experimental results in similar structures [6,7]. The simulations have been performed with a suite of Fortran codes developed completely in-house and exploiting the Lapack linear algebra routines.

Let us define x, y and z the coordinates along the longitudinal, transverse, and orthogonal directions, respectively. We adopt a recursive Green's function approach [12,13]. For the Green's functions, we use a mixed representation: in real space along x and in mode space along y. The effect of the orthogonal magnetic field $\vec{B} = B\hat{z}$ is introduced into the calculation through its corresponding vector potential, chosen according to the following Landau gauge: $\vec{A} = (B\,x)\hat{y}$.

The device is subdivided into a number of transverse slices, chosen in such a way that, within each of them, both the vector and the electric potential can be assumed as approximately independent of x. The first condition translates into a limitation on the magnetic flux threading each slice, which has to be smaller than one flux quantum $h/2e$ (h is Planck's constant, e is the elementary charge).

With these approximations and the adopted gauge, the wave functions $\Psi(x, y)$ within each slice (assuming open boundary conditions along the x direction) have the form

$$\sum_{j=1}^{\infty} \alpha_j A_j \chi_j(y) e^{ik_{x_j} x} + \sum_{l=1}^{\infty} \beta_l A_l \chi_l(y) e^{-ik_{x_l} x}\,, \tag{1}$$

where $\chi_j(y)$ is the transverse wavefunction, k_{x_j} is the longitudinal wave vector, and A_j is a proper normalization coefficient for mode j, α_j and β_l are the coefficients of the linear superposition. Such wave functions are easily evaluated solving a one-dimensional (1D) Schrödinger equation in the absence of magnetic field and multiplying its solutions by a Peierls phase factor.

Once the quantities k_{x_j} and $\chi_j(y)$ have been evaluated for all of the slices, we can compute the Green's function matrix G^0 of the unconnected slices and the matrix V, which represents the coupling between adjacent slices. For the isolated slices, the matrices of Green's functions between pairs of sections of the same slice are diagonal (since no mode-mixing is present) and can be easily evaluated from the wave vectors k_x in the slice, exploiting the known expressions of the Green's function between two generic nodes of an infinite 1D discretized chain [12]. On the other hand, the coupling matrix V can be easily computed from the overlap integrals of the transverse wavefunctions in adjacent slices.

Once the matrices G^0 and V have been computed, the Green's function matrix G of the coupled slices can be found solving the Dyson equation

$$G = G^0 + G^0 V G, \tag{2}$$

or, more efficiently, using recursive relations that can be derived from the application of the Dyson equation between pairs of sections along x (see Reference [12]).

Assuming two semi-infinite leads connected to the left and right ends of the device, we start from the calculation of the Green's functions of the right semi-infinite lead, we compose them with those of the adjacent slice at its left, then we repeat the procedure composing the results with the Green's functions of the successive slice to the left, and so on, until the left semi-infinite lead has also been included. In this way, we find the Green's function matrix between the input and output sections of the simulated region. This quantity is directly related to the transmission matrix of the device [12,13], which can be evaluated and used for the calculation of the conductance with the Landauer-Büttiker formalism:

$$G = \frac{2e^2}{h} \sum_{i,j} T_{ij}, \tag{3}$$

where T_{ij} is the transmission coefficient from mode j to mode i.

In order to exploit the simple relationship existing between the Green's function matrix and the transmission matrix in the absence of a magnetic field, in our simulations, we consider a magnetic field B, which, starting from zero at the outer boundaries of the simulated region, linearly increases towards the value of interest and is kept constant over the active region of the device [14]. Such a smooth transition prevents the introduction of spurious reflections.

Concerning the partition of the device into slices, in the present calculations, the constraint on the magnetic flux threading each slice, which has to be smaller than a flux quantum, is easily satisfied, since we consider a maximum magnetic field of around 400 μT and the width of the cavity is, at most, a few microns. As far as the constraint on the longitudinal invariance of the potential within a single slice is concerned, just a few slices are needed whenever disorder is not considered, since the only potential variations occur between the leads and the constrictions, between the constrictions and the cavity, and between the barrier region and the rest of the cavity. If, instead, disorder is considered, we need to use a much larger number of slices, because the disordered potential has very fast variation. Because the disordered potential is computed on a 10 nm mesh, we use the same mesh in the longitudinal direction for all of the device regions in which disorder is present. Actually, some features of the disordered potential would require an even finer mesh in order to be completely resolved, but this would imply a number of slices so large that the simulation would become impractical, and a 10 nm mesh is anyway a good tradeoff, which allows for a precision that is adequate for all purposes of the present study.

In all of our calculations, we consider a Fermi level of 10 meV, which is typical for the 2DEG obtained by modulation doping at a GaAs/AlGaAs heterointerface. With this Fermi level, the number of propagating modes in the widest structures that we consider ($W = 4$ μm) is around 180. Thus, we include in the simulation a total of 300 transverse modes, with a transverse discretization over 400 points. For the largest and most complex structures that we consider, the computational time that is required for the evaluation of the conductance for 30 values of the magnetic field (averaging

over 40 energy values) is about 10 hrs on a 40 core machine with Intel Xeon E5-2640 processors (Intel, Santa Clara, CA, USA).

As far as the length L_C of the constrictions is concerned, in the absence of disorder, it does not affect the outcome of our simulations, as long as it is large enough to prevent coupling through evanescent modes. However, in the presence of disorder, a longer constriction would not yield a sharp conductance quantization [15]. For all calculations, we considered $L_C = 340$ nm, which, however, would be far too large in the presence of disorder. This is the reason why, in our simulations with the inclusion of disorder, the disordered potential has been introduced only within the length L of the cavity, where the relevant effects in terms of path interference take place.

3. Device Optimization

In this section, we will explore the space of geometrical parameters for the double-dot device, in order to find the values that optimize the operation as magnetic field detector. Intuitively, the effect of magnetic field on conductance will be larger as the cavity size is increased, because a larger magnetic flux is threaded. On the other hand, increasing the cavity size, the average length of the paths is increased, which ultimately leads to dephasing and the disappearance of the enhancement effect. We try tuning parameters around the values that are proposed in Reference [4], in which we had focused on a cavity with a width $W = 4$ μm, a length $L = 8$ μm, a barrier width $W_B = 12$ nm, and a barrier height $H_B = 45$ meV. Our purpose is to verify that this is actually the best tradeoff.

In Figure 2, we report the conductance as a function of the magnetic field in this cavity with a red solid line. Instead, the blue line represents the conductance that would be obtained just with the barrier, without the constrictions, while the green line corresponds to the conductance that would result just as a consequence of the two constrictions, without any barrier. Thus, with respect to the simple barrier alone, in the absence of a magnetic field, the symmetrically placed constrictions raise the conductance to more than one half of what would be reached without any barrier.

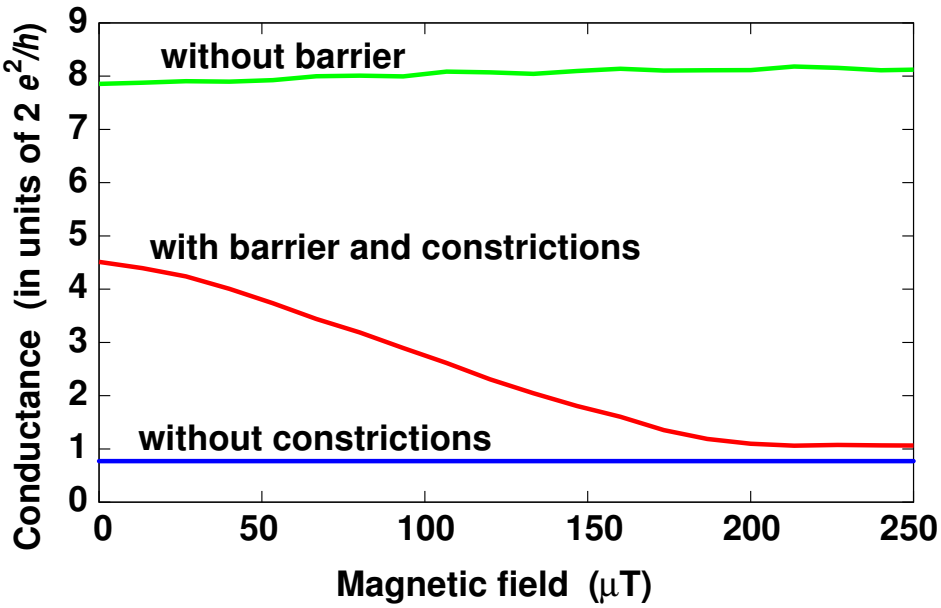

Figure 2. Conductance as a function of the magnetic field for a cavity with a barrier in the middle between the two constrictions; the blue line represents the conductance that would be observed in the absence of the constrictions, while the green curve corresponds to the conductance that would be observed with the constrictions, but without the barrier.

We start our exploration of the parameter space by reducing the cavity width down to $W = 2$ μm. We consider two cavity lengths: $L = 4$ μm and $L = 8$ μ; the results are reported in Figure 3, as a function of magnetic field, for a barrier with a height $H_B = 45$ meV and a width $W_B = 12$ nm. It is

apparent that the conductance variation as a function of the magnetic field is in this case too small, as a result of the decreased flux threading the cavity, therefore it is better to keep the width at 4 μm. A further increase in the sensitivity could be achieved by increasing it above 4 μm, but, as we will discuss later, we would probably reach an excessive average length of the electron paths in the cavity.

We can then study the behavior as a function of cavity length: the results for the simulation of cavities 4 μm wide and for lengths between 4 and 16 μm are shown in Figure 4: we notice that the slope of the conductance vs. magnetic field curve increases with increasing cavity size, but with a length of 16 μm it would be very hard to preserve the required phase coherence. Indeed, the highest low temperature mobility that has been achieved for a 2DEG is around 2×10^7 cm^2/(V s) [16] with a carrier concentration of 2.6×10^{11} cm^{-2}, which is consistent with a Fermi energy of 9.29 meV and a Fermi velocity $v_F = 220.8 \times 10^3$ m/s. Using the expression for the mobility given in Reference [17], we obtain a mean free path $L_0 = \mu m^{\times} v_F / e = 168.3$ μm. Since paths contributing to constructive interference effects may involve several bounces back and forth within the cavity, the diagonal of the cavity (which provides a measure of the distance traveled by the electron between consecutive bounces) should be less than about a tenth of the mean free path, which supports our choice of an 8 μm long and 4 μm wide cavity as a good tradeoff between the total threaded magnetic flux and the preservation of coherence.

We have also investigated the dependence of the conductance vs. magnetic field curve on the barrier thickness, as shown in Figure 5. We notice that, while the thinnest barrier ($W_b = 8$ nm) does not lead to a significant advantage from the point of view of the slope, it leads to a reduced conductance enhancement. On the other hand, for the largest value of W_b, the slope is clearly reduced. Therefore, we have decided to consider $W_B = 12$ nm for the rest of our calculations.

The final parameter to be investigated is the width of the constrictions W_C. In Figure 6, we show the results of simulations of the conductance vs. magnetic field relationship for various values of W_C. We notice that, for $W_C = 100$ nm, we have a reduced conductance and a strongly suppressed slope. As the width is increased up to 200 nm a significant improvement is observed, while with $W_C = 340$ nm or $W_C = 600$ nm the maximum slope is achieved. The difference between the 340 nm and the 600 nm is indeed minimal, and then, for $W_C = 1000$ nm, the conductance curve goes back to a value that is similar to that for $W_C = 200$ nm. Therefore, an optimal behavior is obtained for constriction widths between 340 nm and 600 nm. In the rest of our calculations we will assume $W_C = 340$ nm.

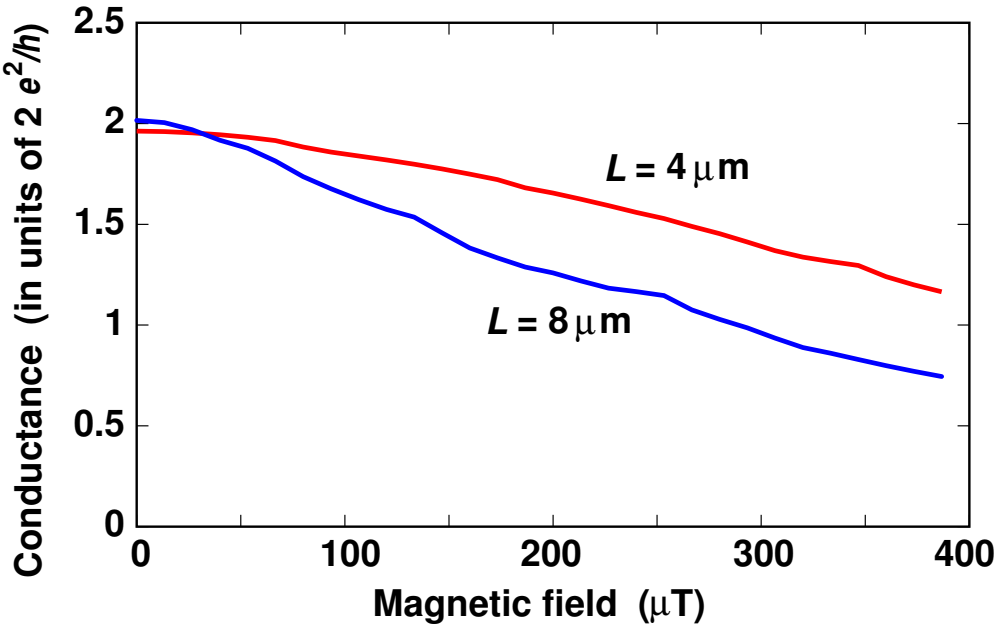

Figure 3. Conductance as a function of the magnetic field for double dots with a width of 2 μm and total lengths between constrictions of 4 μm and of 8 μm. The barrier is 45 meV high and 12 nm thick.

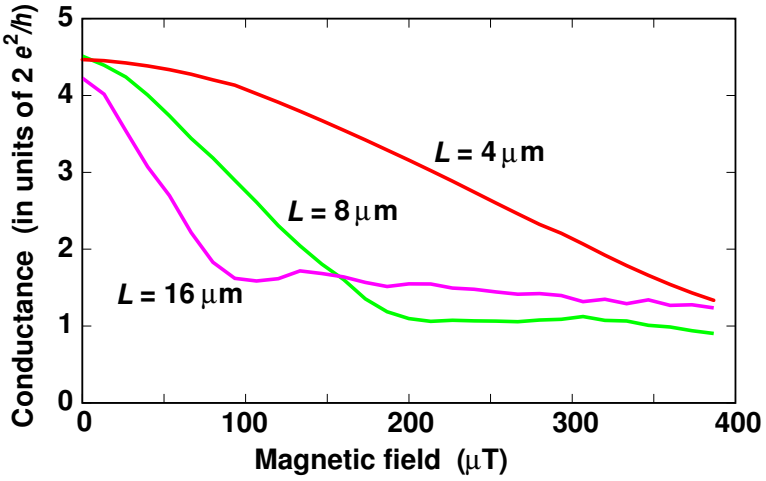

Figure 4. Conductance as a function of the magnetic field for double dots with a width of 4 μm and total lengths between constrictions of 4 μm, 8 μm, and 16 μm. The barrier is 45 meV high and 12 nm thick.

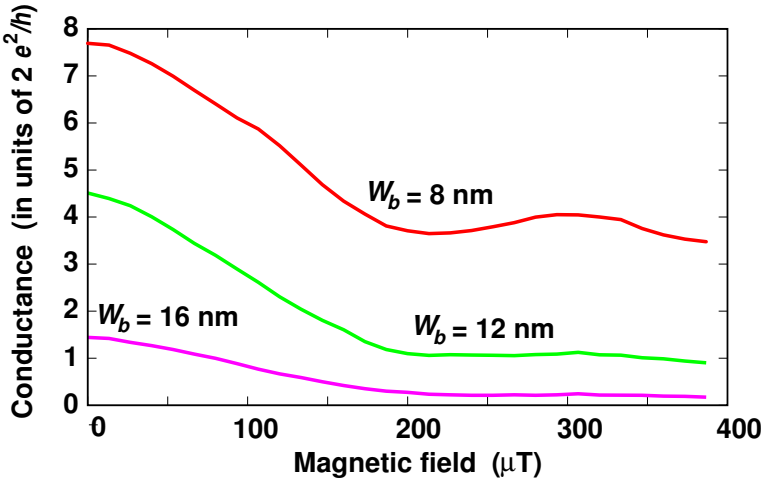

Figure 5. Conductance as a function of the magnetic field for double dots with a width of 4 μm and a total length between constrictions of 8 μm. Results are for three choices of the barrier thickness (the height is 45 meV in all cases): 8 nm, 12 nm, and 16 nm.

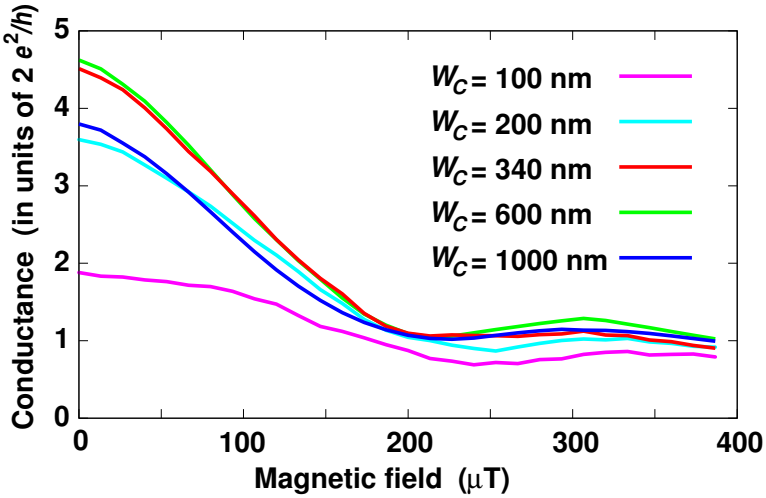

Figure 6. Conductance as a function of the magnetic field for different values of the constriction width W_C. The cavity width is 4 μm and the cavity length is 8 μm. The barrier thickness is 12 nm.

4. Effects of Disorder

The smooth, idealized potential that we have taken into consideration up to now does not exist in practice, mainly because of the action of the randomly located donors and charged impurities. In GaAs/AlGaAs heterostructures, the dopants are in a layer that is physically separated from the 2DEG, in order to achieve the highest possible mobility. While the 2DEG forms in the GaAs bulk, right at the heterointerface with the AlGaAs spacer layer, the donors are instead located on the opposite side of the spacer layer, distributed within an AlGaAs doped layer, which can also be very thin (delta-doping). In a high-mobility heterostructure, the distance between the dopants and the 2DEG can be of a few tens of nanometers. In our calculations we will assume the dopants to be randomly located within a plane parallel to the 2DEG and 40 nm away from it (in the case of delta-doping all of the dopants are within a few nanometers in the vertical direction; therefore, they can be assumed, for the purpose of our calculation, to be within the same plane). However, the resulting potential fluctuations are reduced in amplitude by the screening effect of the 2DEG. An exact calculation of the contribution of each dopant to the potential in the 2DEG would be complex and time consuming, in particular because of the mentioned screening effect.

We have followed a simplified procedure, exploiting the analytical expression derived by Stern and Howard [18] for the electrostatic effect of a donor atom onto a 2DEG with the inclusion of screening, adapting it for the AlGaAs/GaAs material system. At very low temperature, not all of the donors are actually ionized and, in addition, it is reasonable to assume [19] that the distribution of the actually ionized dopants is indeed "less random" than the overall dopant distribution, due to the electrostatic interaction among dopants, which tends to reduce the probability of ionization for an atom that is close to an already ionized one. In order to reduce the complexity of the calculation, we follow an approach that we have developed in Reference [5] that is based on adjusting the density of the dopants, whose electrostatic action onto the 2DEG is then evaluated by means of Stern and Howard's expression, until the expected mean free path is achieved in the 2DEG. The mean free path L_0 can be evaluated by computing the transmission probability in an electron waveguide with the disordered potential. In such a situation, the transmission T is related to the overall length L of the wire, the mean free path L_0, and the number of propagating modes N by the simple relationship [17]

$$T = \frac{NL_0}{L + L_0}\,. \tag{4}$$

We consider an electron waveguide that is 4 μm wide and 8 μm long, in which 184 modes are propagating (for a transverse discretization over 400 points). We find that with a donor density $N_D = 1.2 \times 10^{13}$ m^{-2} we obtain a transmission of 172.8, which corresponds to a mean free path of 123 μm. This is comparable with the value of 168.3 μm that we have reported in Section 3. We have then used such a density to generate a disordered potential within the cavity, and computed the conductance as a function of magnetic field. The results are reported in Figure 7, which includes the conductance vs. magnetic field curve for a few different values of the mean free path. We notice that, as the mean free path decreases, the conductance decreases and the same occurs for the slope of the conductance vs. magnetic field. However, as long as the mean free path is at least about ten times the diagonal of the cavity, the conductance enhancement effect is substantially preserved, and the device is usable as a magnetic field detector.

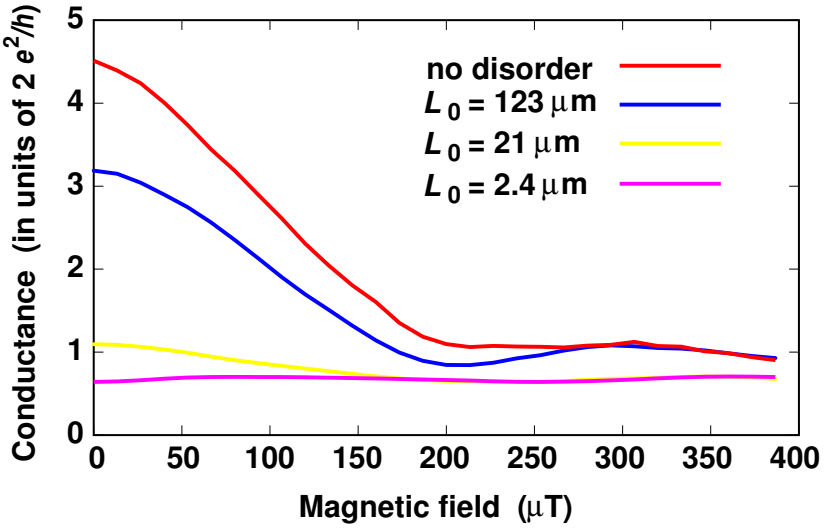

Figure 7. Conductance as a function of the magnetic field in the presence of disorder due to randomly located dopants, for different values of mean free path. The cavity width is 4 μm and the cavity length is 8 μm. The barrier thickness is 12 nm.

5. Evaluation of the Minimum Measurable Magnetic Field

As mentioned in the introduction, we now evaluate the minimum measurable magnetic field level in terms of flicker noise. Both thermal noise and shot noise do not pose fundamental limitations, since the former is constant and the latter only increases linearly with the bias current, as shown in Figure 8. It is only flicker noise (besides generation-recombination noise, which, however is not always present and, in any case, is less relevant than flicker noise at low frequencies) that represents a fundamental limitation.

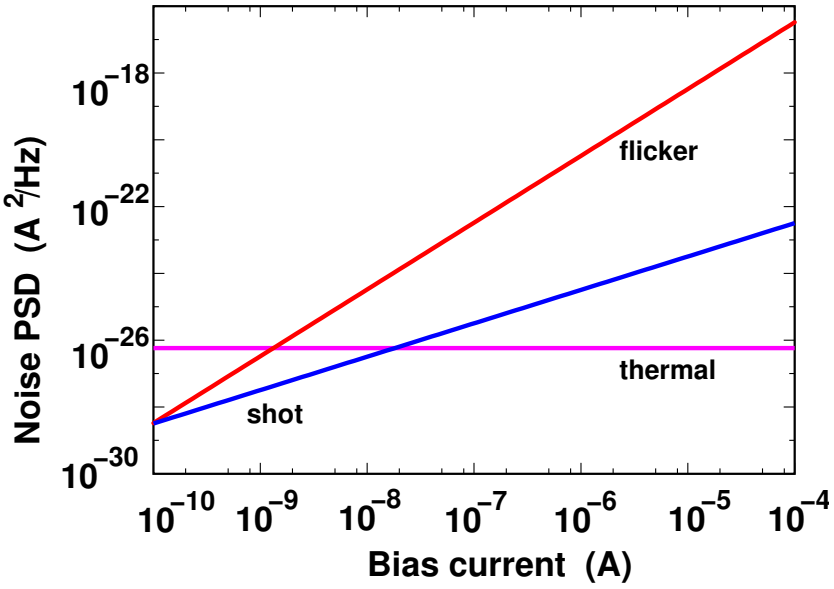

Figure 8. Power spectral density of the different noise components as a function of the bias current.

It is important to point out that, in the presence of flicker noise, the use of a low-pass filter to perform the measurement of the output signal of the detector or, equivalently, of the average over a number of measurements performed at different times do not lead to any improvement of the achieved accuracy, contrary to what happens, for example, with white noise. This has been often overlooked in the literature and it is a consequence of the peculiar properties of the flicker noise power spectral

density. It can be intuitively explained when considering that, if we increase the observation time, we do average over multiple samples, but at the same time we are also including the contribution of lower frequency noise components (which, moreover, have larger amplitudes). However, as long as the observation is performed over a finite amount of time, only frequency components down to about the reciprocal of the observation time contribute to the variance of the measurement. Unfortunately, flicker noise suppression techniques, such as current spinning [20,21], which are instrumental in improving the signal-to-noise ratio in Hall crosses, are not applicable to our device.

Related to this observation is the fact that, in the presence of flicker noise, the sensitivity (defined as the minimum measurable magnetic field) of a magnetic sensor can be expressed in terms of $\mathrm{nT}/\sqrt{\mathrm{Hz}}$ only when we are interested in AC magnetic fields. Instead, if we are interested in the measurement of a DC magnetic field, this is not possible, because integration of the flicker power spectral density over any finite interval including the origin diverges. However, the variance is finite, because of the finite observation time and it can be computed using the Allan variance approach [22,23]. It is to be noted that, in the case of flicker noise, such variance (contrary to what happens, for example, with white noise) does not depend on the observation time and (as previously stated) cannot be reduced by averaging over successive measurements.

We assume that the main flicker noise sources are the constrictions (the regions with the smallest number of charges and, therefore, the noisiest, according to Hooge's formula). In Reference [4], we obtained an estimate of the flicker noise of the constrictions starting from the value of the Hooge constant for a 2DEG in a GaAs/AlGaAs heterostructure. A more reliable estimate can be obtained from the available experimental data on flicker noise in quantum point contacts. In Reference [24], the flicker noise of two quantum point contacts has been measured and for the better performing device $S_V/V^2 = S_I/I^2 \simeq 10^{-10}$ Hz^{-1} at 100 Hz. This corresponds to $S_I = (10^{-8} I^2)/f$; for $I = 1$ μA, we get $S_I = \gamma'/f$, with $\gamma' = 10^{-20}$ A^2. A rigorous calculation of the noise power spectral density in the outer circuit due to the contributions of the two constrictions is complex, due to the ballistic nature of transport. However, it is well known from the literature on mesoscopic cavities [6] that the overall resistance of the cavity simply equals the sum of the resistances R_L and R_R of the two constrictions, due to the decoupling effect of the cavity. Therefore, in the hypothesis of voltage biasing of the device, we can evaluate the total current noise power spectral density $S_{I_{out}}$ in the outside circuit from the schematic presented in Figure 9, where each constriction is represented with a noiseless resistor in parallel with a flicker noise source (S_{I_L} and S_{I_R}), under the reasonable assumption that S_{I_L} and S_{I_R} are uncorrelated:

$$S_{I_{out}} = S_{I_L} \frac{R_R^2}{(R_L + R_R)^2} + S_{I_R} \frac{R_L^2}{(R_L + R_R)^2}, \tag{5}$$

which, in the hypothesis of $R_L = R_R$ and S_{I_L}=$S_{I_R} = S_{I_{fl}}$, yields $S_{I_{out}} = S_{I_{fl}}/2$. Thus, we can consider an overall noise power spectral density $S_{out} = \gamma/f$ with $\gamma = \gamma'/2 = 0.5 \times 10^{-20}$ A^2.

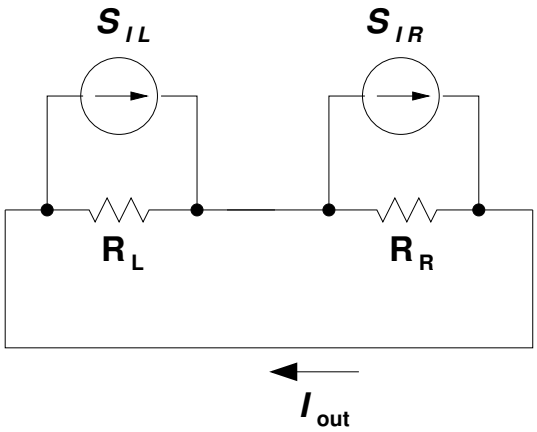

Figure 9. Simplified schematic of the device for noise evaluation.

The standard deviation due to such a level of flicker noise can be computed with the Allan variance approach [22,23], obtaining $\sigma = \sqrt{1.3863\gamma} = 83.26$ pA. Because the derivative of the conductance vs. magnetic field vanishes in the origin, high sensitivity cannot be reached operating around the origin. The shape of the conductance vs. magnetic field curve suggests that the best operating point is in the region of the steepest slope, which can be accessed by adding a permanent magnetic bias of about 100 μT. From the plot relative to a 123 μm mean free path in Figure 7, we can deduce a slope $\Delta G/\Delta B$ of about $-1.26\ \Omega^{-1}$/T. Because the conductance at 100 μT is $G_0 = 0.156\ \mathrm{m}\Omega^{-1}$, the bias voltage that is needed to have a current I_B of 1 μA is $V_B = I_B/G_0 = 6.415$ mV. The current variation ΔI for a magnetic field variation ΔB is given by $\Delta I = V_B(\Delta G/\Delta B)\Delta B$. The current reading for a given applied magnetic field can be assumed to be within 3σ around the expected value; therefore, if we require a relative error around 10%, we need that $|\Delta I| > 10 \times 3\sigma = 30\sigma = 2.498$ nA. This corresponds to a magnetic field variation

$$|\Delta B| = \frac{\left|\frac{\Delta I}{V_B}\right|}{\left|\frac{\Delta G}{\Delta B}\right|} = 309\,\mathrm{nT}\,. \tag{6}$$

Thus, with this approach the minimum measurable magnetic field with a 10% relative error is of the order of 300 nT, with the inclusion of the effect of the disorder associated with a very high-quality two-dimensional electron gas. More, in general, if an η% relative error is required, the minimum measurable magnetic field is of the order of 300 nT$\times(10/\eta)$ (i.e., 3 μT$/\eta$). Comparison with other detectors is not completely straightforward, because, in the literature, the detector performance is often given at frequencies away from DC [25–27] (where flicker noise contributions are less severe) or without an explicit estimate of the relative error, i.e., in terms of the limit of detection (LOD) [28]. For example, an ultra-sensitive NEMS (nanoelectromechanical system) magnetometer [29] has been reported to exhibit a detection limit of 0.8 nT, i.e., at 0.8 nT the detector signal was about equal to the noise. For our detector, this condition should be reached when the standard deviation of the noise equals the signal, i.e., for about 10 nT.

To further reduce the minimum measurable magnetic field, it would be possible to use an AC bias current instead of a DC bias current, while still measuring a DC magnetic field. This is not guaranteed, in principle, to improve the situation, because, in the presence of an AC bias, the flicker noise spectrum would most probably be translated around the bias current frequency. However, an improvement could be achieved by using a lock-in technique for the detection of the Hall signal [30] (however, the situation studied in such a paper is different, with a constant DC bias and an AC magnetic field), which should suppress part of the flicker noise, since it is not correlated with the AC signal.

In actual measurements, particular care should also be devoted to the presence of Earth's magnetic field (i.e., the geomagnetic field), which, in the absence of a proper treatment, would shift the operating point of the sensor into an unusable region. A way around this limitation could be to perform measurements in a magnetically shielded enclosure. Otherwise, the geomagnetic field, which is, in general, known (or, anyway, can be measured with the source under test removed) can be canceled with an opposite homogeneous magnetic field, produced by a solenoid (or with a set of Helmholtz coils, if we want to generate a homogeneous field over an extended volume).

6. Conclusions

We have performed an optimization of the geometrical parameters of a magnetic field detector based on a double dot, which is essentially a cavity divided into two symmetric halves by a potential barrier. We conclude that a good tradeoff between the capability of collecting magnetic flux and the preservation of coherence, which is at the basis of the conductance enhancement effect, is achieved with a 4 μm by 8 μm cavity. We have also included the effect of a random distribution of donors adjusted in such a way as to achieve the same mean free path reported for the best two-dimensional electron gases in GaAs/AlGaAs heterostructures. With optimal geometrical parameters and the application

of a constant magnetic bias, we estimate that a magnetic field variation of around 300 nT can be measured with 10% accuracy. This is a significant improvement over previous estimates, although the performance is not yet as good as that of the best available magnetic field detectors.

Author Contributions: M.M. and P.M.: conceptualization; methodology; software; validation; formal analysis; investigation; resources; data curation; writing—original draft preparation; writing—review & editing; visualization; funding acquisition. S.R.: validation; formal analysis; writing—review & editing; visualization; funding acquisition. All authors have read and agreed to the published version of the manuscript.

Funding: This work was partially supported by the Italian Ministry of Education and Research (MIUR) in the framework of the CrossLab project (Departments of Excellence). ICN2 is funded by the CERCA Programme/Generalitat de Catalunya, and is supported by the Severo Ochoa program from Spanish MINECO (Grant No. SEV-2017-0706).

Conflicts of Interest: The authors declare no conflict of interest.

References

1. Macucci, M.; Marconcini, P. Tunneling enhancement through a barrier surrounded by a mesoscopic cavity. *J. Comput. Electron.* **2007**, *6*, 203–206. [CrossRef]
2. Whitney, R.S.; Marconcini, P.; Macucci, M. Huge conductance peak caused by symmetry in double quantum dots. *Phys. Rev. Lett.* **2009**, *102*, 186802. [CrossRef] [PubMed]
3. Marconcini, P.; Macucci, M. Symmetry-dependent transport behavior of graphene double dots. *J. Appl. Phys.* **2013**, *114*, 163708. [CrossRef]
4. Macucci, M.; Marconcini, P. Study of the Signal to Noise Ratio of a Double-Dot Magnetic Detector. In Proceedings of the 13th IEEE Nanotechnology Materials and Device Conference 2018 (NMDC 2018), Portland, Oregon, USA, 14–17 October 2018; IEEE Publishing: Piscataway, NJ, USA, 2018; article n. 8605875. [CrossRef]
5. Totaro, M.; Marconcini, P.; Logoteta, D.; Macucci, M.; Whitney, R.S. Effect of imperfections on the tunneling enhancement phenomenon in symmetric double quantum dots. *J. Appl. Phys.* **2010**, *107*, 043708. [CrossRef]
6. Oberholzer, S.; Sukhorukov, E.V.; Strunk, C.; Schönenberger, C.; Heinzel, T.; Holland, M. Shot noise by quantum scattering in chaotic cavities. *Phys. Rev. Lett.* **2001**, *86*, 2114–2117. [CrossRef] [PubMed]
7. Oberholzer, S.; Sukhorukov, E.V.; Schönenberger, C. Crossover between classical and quantum shot noise in chaotic cavities. *Nature* **2002**, *415*, 765–767. [CrossRef] [PubMed]
8. Marconcini, P.; Totaro, M.; Basso, G.; Macucci, M. Effect of potential fluctuations on shot noise suppression in mesoscopic cavities. *AIP Adv.* **2013**, *3*, 062131. [CrossRef]
9. Rotter, S.; Aigner, F.; Burgdörfer, J. Statistics of transmission eigenvalues in two-dimensional quantum cavities: Ballistic versus stochastic scattering. *Phys. Rev. B* **2007**, *75*, 125312. [CrossRef]
10. Agam, O.; Aleiner, I.; Larkin, A. Shot Noise in Chaotic Systems: "Classical" to Quantum Crossover. *Phys. Rev. Lett.* **2000**, *85*, 3153–3156. [CrossRef] [PubMed]
11. Marconcini, P.; Macucci, M.; Iannaccone, G.; Pellegrini, B.; Marola, G. Analysis of shot noise suppression in mesoscopic cavities in a magnetic field. *EPL* **2006**, *73*, 574–580. [CrossRef]
12. Sols, F.; Macucci, M.; Ravaioli, U.; Hess, K. Theory for a quantum modulated transistor. *J. Appl. Phys.* **1989**, *66*, 3892–3906. [CrossRef]
13. Macucci, M.; Galick, A.; Ravaioli, U. Quasi-three-dimensional Green's-function simulation of coupled electron waveguides. *Phys. Rev. B* **1995**, *52*, 5210–5220. [CrossRef] [PubMed]
14. Macucci, M.; Marconcini, P. Shot noise suppression due to a magnetic field in disordered conductors. *J. Comput. Electron.* **2015**, *14*, 107–113. [CrossRef]
15. Nixon, J.A.; Davies, J.H.; Baranger, H.U. Breakdown of quantized conductance in point contacts calculated using realistic potentials. *Phys. Rev. B* **1991**, *43*, 12638–12641. [CrossRef] [PubMed]
16. Radu, I.P.; Miller, J.B.; Marcus, C.M.; Kastner, M.A.; Pfeiffer, L.N.; West, K.W. Quasi-Particle Properties from Tunneling in the $\nu = 5/2$ Fractional Quantum Hall State. *Science* **2008**, *320*, 899–902. [CrossRef] [PubMed]
17. Datta, S. *Electronic Transport in Mesoscopic Systems*; Cambridge University Press: Cambridge, UK, 1995; pp. 9, 62–63; ISBN: 0521416043.
18. Stern, F.; Howard, W.E. Properties of Semiconductor Surface Inversion Layers in the Electric Quantum Limit. *Phys. Rev.* **1967**, *163*, 816–835. [CrossRef]

19. Totaro, M.; Marconcini, P.; Macucci, M. Ionized donor reordering in typical heterostructures. In Proceedings of the 14th International Workshop on Computational Electronics 2010 (IWCE 2010), Pisa, Italy, 26–29 October 2010; IEEE Publishing: Piscataway, NJ, USA, 2010; article n. 5677988; pp. 175–178. [CrossRef]
20. Kerlain, A.; Mosser, V. Dynamic low-frequency noise cancellation in quantum well Hall sensors (QWHS). *Sens. Actuator A-Phys.* **2008**, *142*, 528–532. [CrossRef]
21. Mosser, V.; Matringe, N.; Haddab, Y. A Spinning Current Circuit for Hall Measurements Down to the Nanotesla Range. *IEEE Trans. Instrum. Meas.* **2017**, *66*, 637–650. [CrossRef]
22. Allan, D.W. Statistics of atomic frequency standards. *Proc. IEEE* **1966**, *54*, 221–230. [CrossRef]
23. Giusi, G.; Scandurra, G.; Ciofi, C.; Pace, C. Long term stability estimation of DC electrical source from low frequency noise measurements. In *Proc. SPIE*, Volume 5470 (*Noise in Devices and Circuits II*); SPIE Press: Bellingham, WA, USA, 2004; pp. 470–479. [CrossRef]
24. Li, Y.P.; Tsui, D.C.; Heremans, J.J.; Simmons, J.A.; Weimann, G.W. Low-frequency noise in transport through quantum point contacts. *Appl. Phys. Lett.* **1990**, *57*, 774–776. [CrossRef]
25. Xu, H.; Huang, L.; Zhang, Z.; Chen, B.; Zhong, H.; Peng, L.-M. Flicker noise and magnetic resolution of graphene hall sensors at low frequency. *Appl. Phys. Lett.* **2013**, *103*, 112405. [CrossRef]
26. Huang, L.; Zhang, Z.; Chen, B.; Ma, X.; Zhong, H.; Peng, L.-M. Ultra-sensitive graphene Hall elements. *Appl. Phys. Lett.* **2014**, *104*, 183106. [CrossRef]
27. Díaz-Michelena, M. Small Magnetic Sensors for Space Applications. *Sensors* **2009**, *9*, 2271–2288. [CrossRef] [PubMed]
28. Röbisch, V.; Salzer, S.; Urs, N.O.; Reermann, J.; Yarar, E.; Piorra, A.; Kirchhof, C.; Lage, E.; Höft, M.; Schmidt, G.U.; et al. Pushing the detection limit of thin film magnetoelectric heterostructures. *J. Mater. Res.* **2017**, *32*, 1009–1019. [CrossRef]
29. Li, M.; Matyushov, A.; Dong, C.; Chen, H.; Lin, H.; Nan, T.; Qian, Z.; Rinaldi, M.; Lin, Y.; Sun, N.X. Ultra-sensitive NEMS magnetoelectric sensor for picotesla DC magnetic field detection. *Appl. Phys. Lett.* **2017**, *110*, 143510. [CrossRef]
30. Shimazu, Y.; Iwabuchi, T.; Arai, K.; Shioya, I. Hall effect measurements using low ac magnetic fields and lock-in technique on field-effect transistors with molybdenum disulfide channels. *Phys. Lett. A* **2020**, *384*, 126073. [CrossRef]